Analysis of mesoscopic patterns formed by the Au-induced faceting of vicinal Si(001)

2006 J. Phys.: Condens. Matter 18 S1

(http://iopscience.iop.org/0953-8984/18/13/S01)

INSTITUTE OF PHYSICS PUBLISHING JOURNAL OF PHYSICS: CONDENSED MATTER

J. Phys.: Condens. Matter **18** (2006) S1–S15 doi:10.1088/0953-8984/18/13/S01

Analysis of mesoscopic patterns formed by the Au-induced faceting of vicinal Si(001)

Frank-Joachim Meyer zu Heringdorf[1]

Institut für Experimentelle Physik, Universität Duisburg-Essen, Lotharstrasse 1, 47057 Duisburg, Germany

E-mail: meyerzh@uni-due.de

Received 25 January 2006, in final form 26 February 2006
Published 13 March 2006
Online at stacks.iop.org/JPhysCM/18/S1

Abstract

Vicinal Si(001) surfaces with ≈4° miscut toward [110] consist of ordered terraces that are separated by a double step every 4 nm. Adsorption of Au at 800–900 °C changes the step morphology dramatically: after a critical Au coverage of 1/3 ML is reached, Au condenses from an initially formed lattice gas into a (5 × 3.2) reconstruction on newly formed (001) terraces. The steps of the vicinal surface are accumulated in irregular step bunches to conserve the macroscopic miscut. With increasing Au coverage the step bunches are transformed into well defined facets. The ultimate facet orientation depends on the adsorption temperature, although at temperatures above $T = 800\,^{\circ}\mathrm{C}$ only (001) terraces and (119) facets are observed. Depending on the deposition temperature, the terraces and facets exhibit a periodicity from 200 nm to 4 μm and a structural length of up to several millimetres. Illumination with white light under grazing incidence results in a colourful striped pattern in an optical microscope. A novel *in situ* light diffraction experiment is presented, that is perfectly matched to the mesoscopic dimensions of the faceted surfaces. Illumination with a He–Ne laser during and after deposition results in complex diffraction patterns that can be used to estimate the length of the terraces. The temperature dependence of the terrace length shows an Arrhenius behaviour with an activation energy of $E_A \approx 2.8$ eV during the initial stages of the faceting; at $T = 825\,^{\circ}\mathrm{C}$ the terraces extend with a constant velocity of 30 $\mu\mathrm{m\,s^{-1}}$. This value is in excellent agreement with earlier low energy electron microscopy measurements.

(Some figures in this article are in colour only in the electronic version)

[1] http://www.iep.physik.uni-essen.de/hvh

1. Introduction

The fabrication of nanoscale structures and their self-organized arrangement on surfaces is one of the most challenging tasks in modern semiconductor research. In particular, adsorbate induced faceting [1, 2] and step arrangement control [3, 4] of vicinal single-crystalline semiconductor surfaces is a key technique for the self-organization of one-dimensional mesoscopic structures that can be used as a template for selective deposition under grazing incidence in subsequent processing steps. The width, height, and length of the resulting structures, however, is greatly affected by the specific properties of the template. Whether a particular material combination offers a suitable template depends on the adsorbate induced modification of the surface free energy [5], the changes in surface stress [6], modifications of the step energy [7], and the step–step interaction [8]. While many examples are known where adsorbates induce faceting or step bunching of oriented and vicinal Si surfaces [9–13], usually the correlation lengths are too small to use the faceted surfaces as templates for selective deposition. In contrast, sub-monolayer adsorption of Au on ≈4° vicinal Si(001) surfaces at temperatures between 800 and 900 °C, however, results in the formation of extremely straight and elongated 'super'-terraces with a length of up to several millimetres and an average separation from 200 nm to 4 μm. On a 4.2° vicinal Si(001) surface, a facet separation of only 1 μm already causes a height undulation of almost 40 nm. Structures of such size can easily be used as templates for selective deposition, as has already been demonstrated in the past [14].

The kinetics and the microscopic driving forces for self-organized structure formation are accessible to the standard tools of surface science, and section 3 of this publication reviews the kinetics of the faceting. Section 5 is devoted to a new experiment, that allows the determination of the long-range mesoscopic order of the structures. Since the occurring length scales range from nanometres to millimetres they are accessible to light scattering, and it will be shown here how the simple diffraction of a laser during the faceting of the surface gives insight into the kinetics on a mesoscopic length scale.

2. Experimental details

Most of the experiments presented here were performed in a dedicated ultrahigh vacuum (UHV) deposition chamber with a base pressure of $p = 1 \times 10^{-10}$ mbar (MBE chamber). The samples were analysed *in situ* before, during and after faceting with spot-profile-analysing low energy electron diffraction (SPA-LEED) [15]. The *in situ* light diffraction experiments were performed in the same chamber.

In contrast, the *in situ* low energy electron microscopy (LEEM) experiments were performed at the synchrotron light source ELETTRA in Trieste (Italy), using an ELMITEC spectroscopic photo-emission LEEM prototype (SPE-LEEM) [16]. Si(001) samples with a miscut of 4.2° in the [110] direction were cut from a Si wafer, wiped off with ethanol and degassed overnight at $T \approx 600\,^{\circ}\mathrm{C}$ in high vacuum ($p < 10^{-7}$ mbar). The samples were then transferred to UHV and stripped of their native oxide by repeated flash-annealing at temperatures of up to $T = 1250\,^{\circ}\mathrm{C}$. In the MBE chamber the samples were resistively heated, while in the SPE-LEEM the samples were heated by electron bombardment. In both set-ups, Au was deposited at a sample temperature above $T = 800\,^{\circ}\mathrm{C}$ from a water-cooled home-built electron-beam evaporator with a graphite crucible.

3. The kinetics of Au induced faceting

For a Si(001) surface with a miscut of ≈4° in the [110] direction, the anisotropic surface stress of the dimers in the (2×1) reconstruction leads to the formation of a double step arrangement on

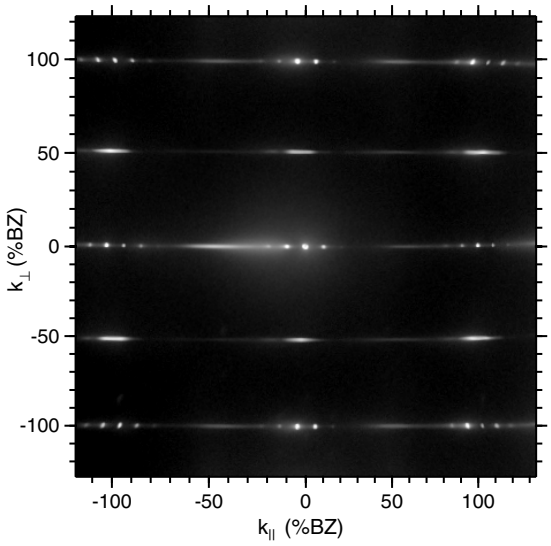

Figure 1. SPA-LEED pattern of the initial vicinal Si(001) surface. Only one of the two possible (2 × 1) and (1 × 2) reconstruction domains is visible. The spot-splitting of the integer order spots is an indication of an ordered step array.

the surface [8]. Figure 1 shows a SPA-LEED pattern of such a surface. The diffraction pattern clearly shows that only one of the two possible (2 × 1) and (1 × 2) domains exists, which is an indication of double steps on the surface. Furthermore, the double steps are arranged in a very regular sequence. The convolution of the atomic surface lattice with an ordered super-lattice of (double) steps leads to a spot-splitting of all integer order spots in LEED [17]. From the spot-splitting, the average distance between the double steps can be calculated to be 4 nm, which agrees well with the separation as expected from the vicinality of the sample or as determined by scanning tunnelling microscopy (STM).

Deposition of Au on this surface at elevated temperatures leads to a rearrangement of the steps on the surface and faceting. Figure 2 shows LEEM images recorded during adsorption of Au at $T = 800\,^{\circ}\mathrm{C}$ [14]. After the shutter is opened, initially no change on the surface is visible since Au is adsorbed on the surface in a lattice gas. Only after a coverage of about one-third of a monolayer is reached [18] do bright elongated features become visible in the LEEM (figure 2(a)). Under the bright-field imaging conditions of the LEEM, these features represent (001)-type terraces. SPA-LEED and STM show that the terraces are covered with a complex ordered domain-wall reconstruction [19]. This reconstruction is commonly referred to as (5 × 3.2) [20]. The reconstructed (001) terraces extend along the step direction of the substrate and cause step bunching as they grow.

In diffraction, the inclination angle of the areas between the terraces can be determined by recording of scans in the direction perpendicular to the steps. In the so-called external geometry of the SPA-LEED [17] this is even possible during deposition. Figure 3 shows the assembly of a sequence of linescans into a grey-scale representation with logarithmic scaling. This provides valuable information about the bunched steps [20]. Before deposition, only the split spots of the regular double-step sequence are visible at the top of figure 3. After the shutter is opened at t_0, the form-factor for diffraction is changed by the Au lattice gas, resulting in an increase of the scattered intensity of the '4° spot A'. At t_1, the first (001) terraces are formed and contribute to the spot labelled '(00)' in figure 3. The (5×3.2) reconstruction on these terraces causes spots C

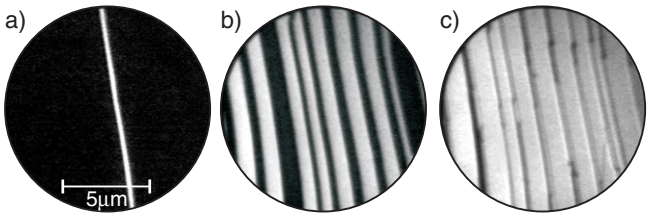

Figure 2. Bright-field LEEM images of different stages of the Au-induced faceting at $T = 800\,^{\circ}\mathrm{C}$. (a) Condensation of the first terrace, (b) step-bands with maximum inclination angle, (c) transition of step-bands to (119) facets.

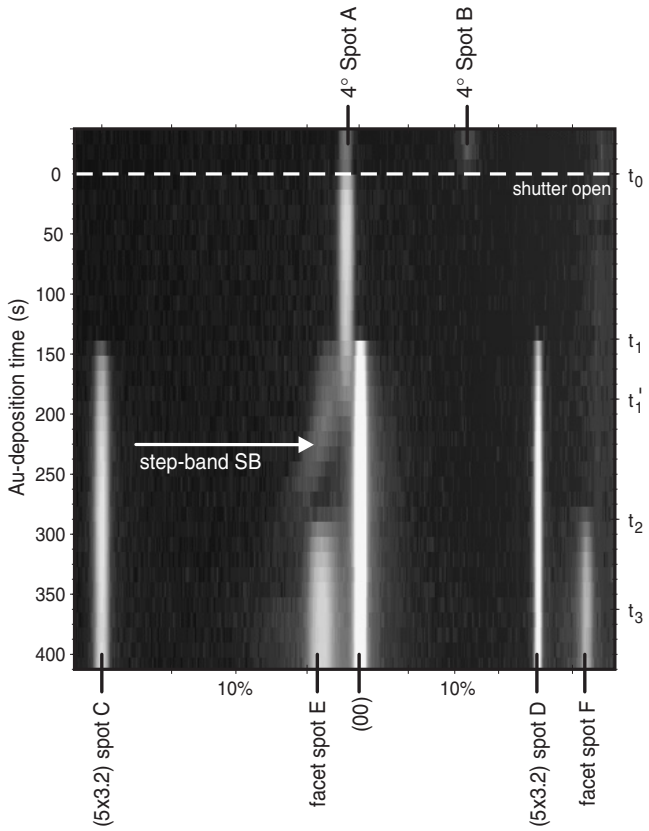

Figure 3. Time dependence of diffraction profiles perpendicular to the step edges during Au deposition. Deposition starts at t_0. First (001) terraces are formed at t_1. The step band angle increases from t_1' to t_2. At t_2 the step band is converted into (119) facets. At t_3 the faceting is complete and further deposition of Au leads to cluster formation.

and D. The newly formed step bunches in the vicinity of the (001) terraces are labelled as 'step-band SB'. The step-band must be formed along with the terraces to conserve the macroscopic miscut of the sample.

While the (001) terraces are well separated, the step-band surrounding the terraces has an average angle of only $\approx 8^{\circ}$. As the terraces grow and more terraces are formed, however (figure 2(b)), the angle of the stepped areas between the terraces increases. Accordingly, at

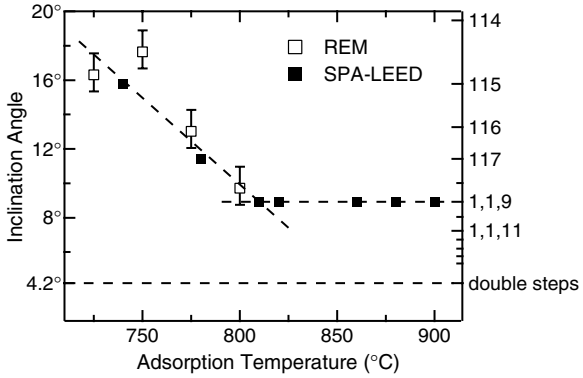

Figure 4. Dependence of the final facet angle on the adsorption temperature. At temperatures below $T = 800\,^{\circ}\mathrm{C}$ the step-band is not fully converted to (119) facets; rather, the facet angle locks into local minima of the surface free energy. Reflection electron microscopy (REM) data taken from [21].

t_1' the SB spot in figure 3 slowly shifts to higher angles. This continues until the step-band reaches an inclination angle of about 15° at (t_2) and new spots appear. Facet spot E indicates a conversion of the rough and steep step-band into ordered facets (t_3). Spot F is an indication of a reconstruction on these facets. In LEEM, the transition from stepped areas to ordered facets is also visible: in figure 2(c) the dark step-band has turned into light-grey faceted areas. The surprising result that the facet angle is lower than the maximum step-band angle of 15° has been explained by the balance of surface free energies of the Au covered and uncovered surface areas [21].

After the faceting is complete at t_3 in figure 3, the diffraction pattern does not change any more, even if the deposition is continued. *Ex situ* scanning electron microscopy (SEM) reveals that excess Au is collected in clusters on the surface [22].

The faceting can be summarized as a two step-process. During the first stage, (001) terraces are formed that cause step bunching in the separating areas. The terraces form a sink for the Au atoms in their surroundings that thermally diffuse onto the existing terraces. These Au atoms are immediately incorporated into the (5×3.2) reconstruction on the terraces. In the depleted areas between the terraces, the local Au coverage is below the critical coverage needed for formation of new (001) terraces [23]. In this respect, the thermally activated diffusion of Au on the surface is responsible for the long-range structure formation.

Only when the step-bands become too steep and the energy gained by further extension of the (001) terrace does not compensate the energy needed to push the step-band to an even higher inclination angle, Au adsorbs on the step-band and transforms it into defined facets with a lower inclination angle.

Depending on the adsorption temperature, however, the second transition might not be complete, as illustrated in figure 4. Here the resulting facet angle is plotted over the adsorption temperature [18]. While the surface would prefer to form ordered (119) facets with a inclination angle of 8.9°, at adsorption temperatures below $T = 810\,^{\circ}\mathrm{C}$ the facet angle locks into local minima of the surface free energy, with facet orientations of higher inclination angles such as (115) and (117). Only at high temperatures is the thermodynamic equilibrium reached and extremely well ordered (119) facets are formed.

The reciprocal space maps [24] in figure 5 compare the step structure of the initial 4.2° vicinal surface (figure 5(a)) and a faceted surface that was generated at high

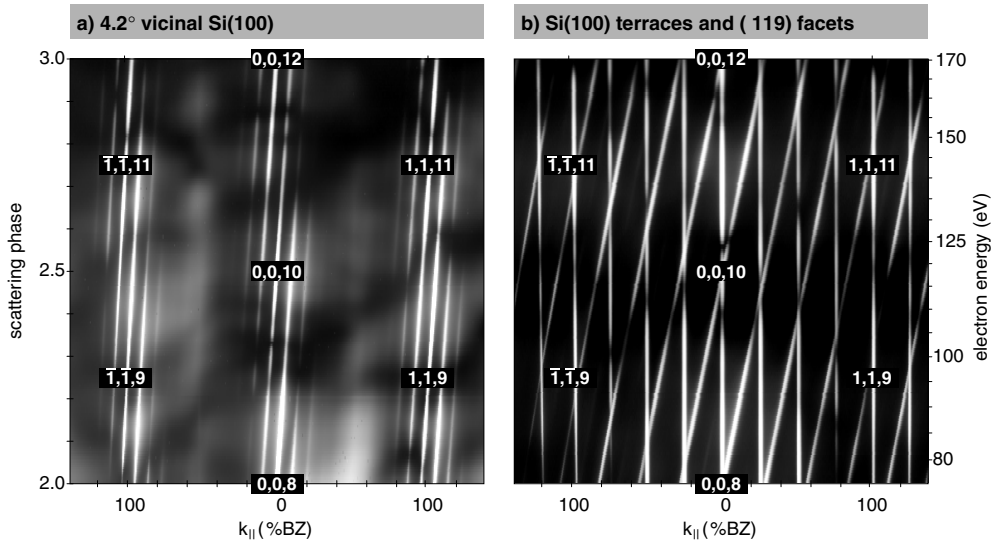

Figure 5. Reciprocal space maps of (a) the initial 4.2° miscut surface and (b) the surface after completed faceting at $T > 800\,^{\circ}$C. The maps directly visualize the reciprocal lattice rods of the surfaces.

temperatures (5(b)). The initial surface shows lattice rods of the regular double-step train that are inclined by 4.2° with respect to the vertical (001) orientation. The lattice rods are only visible in the immediate vicinity of the (001) lattice rods as expected for this type of surface. Panel 5(b) shows the surface after completed faceting at $T > 800\,^{\circ}$C. Pronounced and sharp (001) rods from the (001) terraces are now visible alongside equally sharp (119) facet rods. The LEEM images in figure 2 already indicate that the terraces and facets have an average width of more than 100 nm, and accordingly the width of the lattice rods in figure 5(b) is determined by the transfer width of the SPA-LEED.

The described behaviour of multiple rearrangements during adsorption seems to be a rather general concept when it comes to faceting of vicinal Si(001) surfaces. Similar experimental results were found for different miscuts of Si(001) [25], but also for stepped Si(111) [12], and other Si surfaces. The specifics of the faceting can be more complicated, however, and in the case of a Si (hhm) $(m/h = 1.4 - 1.5)$ surface five different intermediate steps were reported [13].

Figure 6 summarizes the different steps of rearrangement during the adsorption of Au on the vicinal Si(001) surface. Starting with the regular double-stepped 4.2° miscut surface (figure 6(a)), Au initially forms a disordered lattice gas on the surface. After a critical coverage of $\approx 1/3$ of a monolayer is reached, (001) terraces are formed that cause step bunching in their vicinity in order to conserve the macroscopic miscut of the sample (figure 6(b)). As the terraces grow, the inclination angle of the step bunches increases in response (figures 6(c), (d)). This process ends once an inclination angle of the step-band of about 15° is reached (figure 6(e)). Further deposition triggers a rearrangement of the steep step-band to facets with a lower inclination angle. Unless the rearrangement is kinetically limited by low adsorption temperatures, the final facet orientation is (119). After deposition of $\approx 2/3$ of a monolayer of Au the faceting is complete. Continued deposition leaves the surface morphology unchanged and three-dimensional islands are formed on the surface. Whether these islands only consist of Au or also contain Si has not been clarified yet.

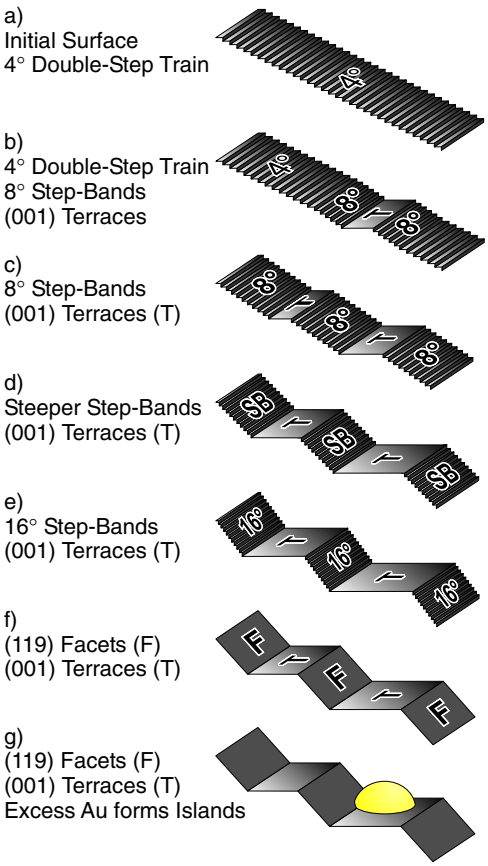

Figure 6. Sketch of the different stages of the faceting. (a) The initial miscut Si(001) surface. (b) Formation of (001) terraces and local step-bunching. (c) Formation of more terraces with increasing step-band angle. (d) Extension of the terraces with increasing step-band angle. (e) Maximum inclination angle of the step-band. (f) Faceting with (119) facets. (g) Excess Au forms islands on the surface and leaves the morphology of the faceted surface intact.

4. The dimension of the superterraces

The Au-induced faceting leaves the surface with some rather mesoscopic structures as the Au depleted areas around each terrace introduce some long range order: in the surrounding of a terrace the Au coverage lies below the critical coverage necessary for formation of a new terrace. The distance between the terraces is then given by the size of the depleted areas, which in turn is determined by the Au diffusion length. Since the diffusion length is strongly dependent on the temperature, the average spacing between the terraces should be temperature dependent as well. *Ex situ* scanning electron microscopy (SEM) shows that depending on the adsorption temperature the average terrace separation varies between 200 nm (low adsorption temperature) and 4 μm (high adsorption temperature). Such structures are in the range of the wavelength of visible light, and if they are sufficiently ordered they should act as a blaze grating. Figure 7 shows images taken with a regular optical microscope while illuminating with white light under grazing incidence. The colourful striped patterns are a representation of the gratings on the surface. The pattern formed at lower adsorption temperature (figure 7(a)) is less ordered than the pattern in (figure 7(b)), formed at higher temperature without the kinetic limitation

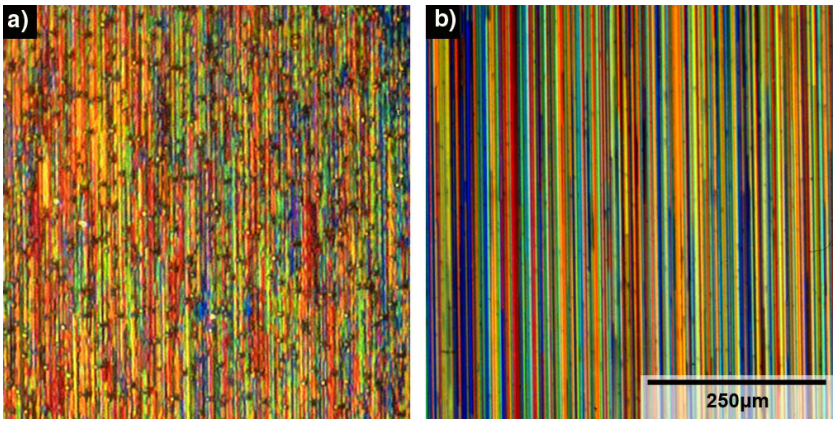

Figure 7. Microscope images of faceted surfaces under grazing-incidence illumination with white light: (a) faceting at $T < 800\,^{\circ}\mathrm{C}$; (b) faceting at $T > 800\,^{\circ}\mathrm{C}$. The colour in the patterns originates from Fourier-filtering of the spectral components by the microscope aperture.

for the facet orientation. Not only is the lattice constant in figure 7(b) obviously larger, but also the coloured stripes that are a fingerprint of the terraces are much longer. Faceting at high temperatures can apparently lead to millimetre long structures and sometimes the terraces extend over the whole sample surface (5 mm).

An evaluation of figure 7 brings up the question why the patterns are not simply a microscope image of the surface structure but consist of coloured stripes. A slightly disordered grating will scatter different wavelengths of the illuminating light into different angles, depending on the position on the sample and the local lattice constant of the grating. The entrance aperture of the microscope's objective lens, however, cuts out a fixed angular section from the diffraction pattern. For some areas on the sample, red or blue components of the spectrum are scattered to angles that do not lie within this observed angular regime. These colours are missing from the spectrum and thus are responsible for the colourful striped patterns.

If the simple adsorption of Au already leads to the self-organization of a mesoscopic pattern that acts as a grating for visible light, it should also be possible to analyse the formation of the grating *in situ* during deposition by using light scattering techniques.

5. *In situ* light scattering

Figure 8 shows the set-up of a novel experiment to analyse the light scattering in detail during deposition. As before, the sample is mounted in the UHV chamber and is heated during deposition. A HeNe laser (5 mW, >99% TEM_{00}) is mounted outside the UHV and the beam is space-filtered to obtain a Gaussian beam shape. The laser beam enters the vacuum chamber through a standard UHV window, is reflected at the sample surface, and can be monitored outside the UHV (zeroth order). In addition, the blaze grating on the sample creates a highly anisotropic diffraction pattern during the faceting. In particular, the pattern is distributed in a small angular regime along the terraces (vertical direction). In the direction perpendicular to the terraces (horizontal direction), the pattern almost fills the complete half-space but has a pronounced intensity modulation that defines a broad first order maximum.

The complete diffraction pattern consists of a huge number of spots that represent a fingerprint of the specific structure on the sample. Flash annealing and repeated adsorption

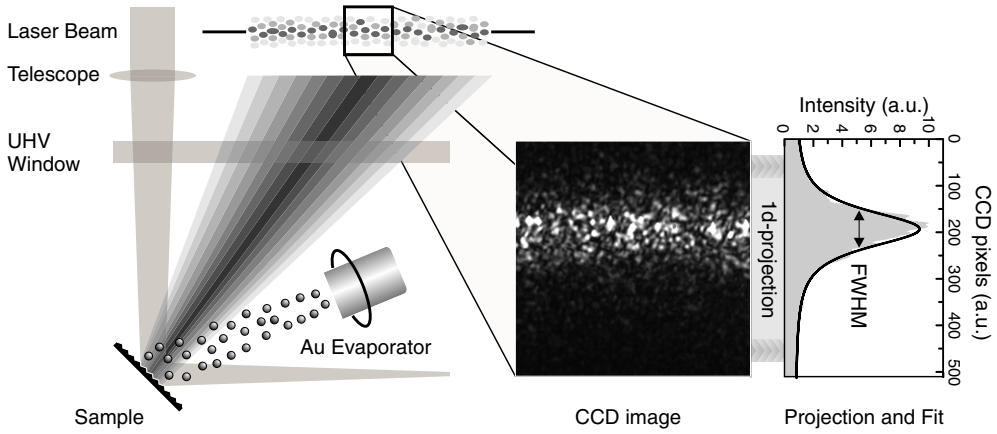

Figure 8. Set-up of the *in situ* light-scattering experiment. During Au deposition a HeNe laser beam is directed onto the sample. The faceted sample creates a complex diffraction pattern, which is very broad in the direction perpendicular to the terraces but has a limited width along the terraces. A section of the pattern is recorded with a CCD camera. For some of the data analysis, the pattern is averaged in the direction perpendicular to the terraces.

of Au changes the position of every single diffraction spot of the pattern from experiment to experiment, while the (horizontal) position of the broad first maximum and the (vertical) width of the pattern along the terraces are reproduced from experiment to experiment as long as the deposition temperature and rate are not changed.

The geometry of the incidence angle of the laser was chosen so that most of the diffraction pattern passes the UHV window and that the intensity of the broad first maximum and the width of the pattern can be analysed during growth. A cooled, slow-scan scientific CCD camera was used to record an area of $1.2^\circ \times 1.2^\circ$ of the diffraction pattern. A typical CCD image is shown in the centre of figure 8. While the camera only records a fraction of the diffraction pattern in the (horizontal) direction perpendicular to the terraces, along the terraces (vertical direction) usually the whole pattern is recorded.

Figure 9 shows how the diffraction pattern develops during faceting at a substrate temperature of $T = 825\,^\circ$C. Panels (a)–(d) of figure 9 show CCD images at different stages of the faceting. The integral intensity of the CCD images is shown at the bottom of figure 9. The camera is placed at the location of the expected broad first order maximum, and although the diffraction pattern does not completely fit onto the CCD chip the signal is a relative measure of the total diffracted intensity. After the deposition is started and the initial dead time during formation of the Au lattice gas has passed, the integral diffracted intensity increases linearly with time. This behaviour is similar to that observed in SPA-LEED [20], and was previously interpreted as a linear increase of the relative surface area of diffracting terraces with coverage. By comparing the light-diffraction curve to the SPA-LEED data, one can expect the step-band formation to be completed at $t \approx 130$ s. The shutter was closed immediately after recording of panel (d) of figure 9, and the slow decay of the integral intensity is due to slow desorption of Au and the transformation of the surface back to double steps.

A careful comparison of panels (b)–(d) in figure 9 indicates that although the integral intensity of the patterns in (c) and (d) is higher, most spots in the pattern have not changed their position. If the data are viewed as a movie, some slight spot movement is apparent during the initial phase of the faceting, but at later stages the pattern remains constant and only the spot intensities change.

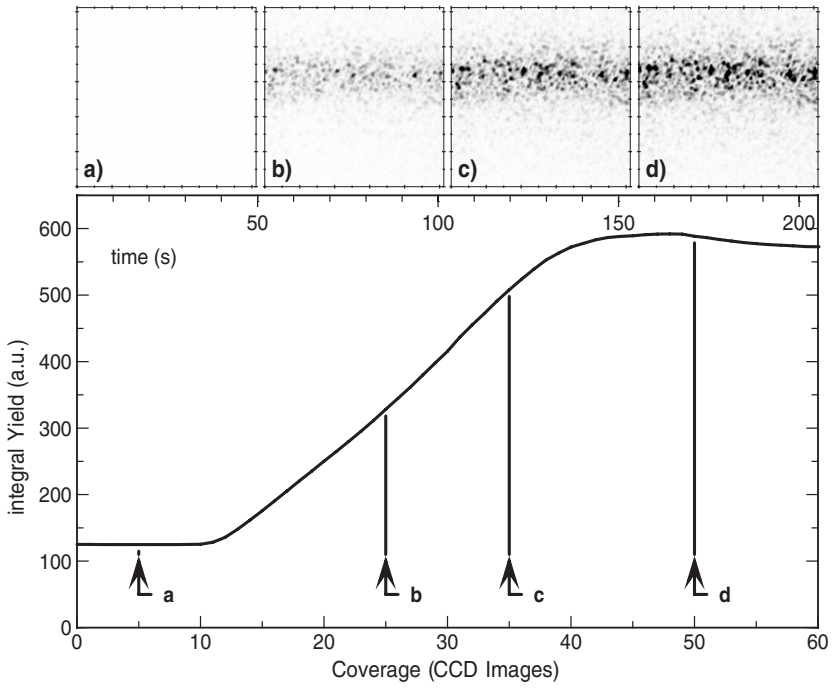

Figure 9. Integral intensity of the light scattering pattern during deposition and CCD images at different stages of the faceting. (a) Before terrace formation, (b) during an early stage of the faceting, (c) during a later stage of the faceting, and (d) after the faceting is complete. The deposition was stopped after recording of pattern (d).

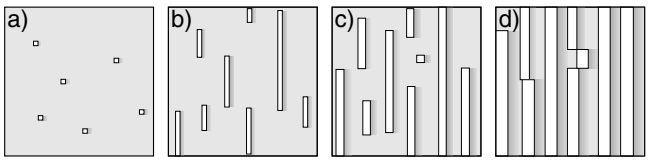

Figure 10. Model for the mesoscopic pattern formation. (a) Initial terrace formation determines the pattern. (b)–(d) The terraces expand along the steps and perpendicular to the steps. The correlation function is not changed.

That the fine structure of the diffraction pattern does not change during the faceting is an indication that the terrace arrangement is already fixed during the initial stages of the deposition as illustrated in figure 10. Some terraces are formed on the surface (figure 10(a)) and extend very quickly along the steps of the original substrate (figure 10(b)). While the terraces grow, their distribution does not change significantly and the spot positions in the diffraction pattern should not change either. As the extension of the terraces proceeds (figure 10(c)), the terraces also slowly gain width as they push the step-band towards higher inclination angles. In figure 10(d) the faceting is complete, and although the terraces are now much larger and separated by (119) facets the distribution of the terraces is still unchanged. It is important to note that this model of the faceting process is consistent with SPA-LEED, LEEM, and light scattering experiments. Incorporation of this model into a computer simulation [23] leads to surfaces with similar simulated diffraction patterns [21].

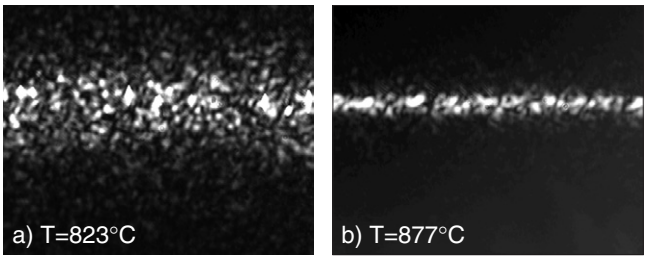

Figure 11. CCD patterns obtained as sketched in figure 8 after faceting at different temperatures.

While the fine structure of the pattern does not change throughout a single experiment, the pattern can become quite different if the experimental conditions are changed. Figure 11 shows two patterns after Au induced faceting at the same deposition rate and different deposition temperatures. The pattern at the higher temperature is much narrower. Panel (a) in figure 11 is more representative of a condition as in figure 7(a) and panel (b) in figure 11 is more representative of a condition as in figure 7(b). While it seems obvious that a narrower pattern is an indication of longer terraces, it is questionable how to extract the terrace length from the pattern.

To correctly predict the pattern for a given surface, one would need knowledge about the exact distribution of terraces on the sample and about the precise interaction of light with an Au-covered Si surface. But neither the distribution function nor the exact scattering conditions are known.

Using a very simple approach, however, allows one to estimate at least an approximate average value for the terrace length from the pattern: if only one terrace was present on the surface, the situation could be treated as diffraction of light at a single scatterer, i.e. at a slit. Adding a second terrace of the same size would change the situation. If the two slits were well separated, the pattern would resemble the incoherent overlay of two diffraction patterns. In contrast, if the terraces were located in close proximity, an additional double-slit contribution would have to be included. As a third terrace would have different distances to the first and the second terrace, the pattern would be the pair-correlation of the three terraces. If more terraces are added, one needs to make assumptions about their size and spatial distribution to correctly predict the diffraction pattern.

Although the distribution function of the terraces is unknown, the intensity of the diffraction pattern is still convoluted with the diffraction pattern of a single terrace, i.e. the slit, just as the convolution of the double-step sequence with a single Si(001) terrace limits the scattered intensity to the vicinity of the (001) rod in figure 5(a). Averaging the pattern in the horizontal direction, perpendicular to the steps (as sketched in figure 8) removes the specific information of the grating and only leaves the average length distribution of the terraces. In this simple 1D approximation, the average terrace size can then be extracted from the full width at half maximum (FWHM) of the averaged pattern within a slit-model. For a single slit, the normalized intensity distribution is well known [26]

$$I(\delta(\theta)) = \frac{\sin^2(\delta)}{\delta^2} \qquad \text{with } \delta(\theta) = \frac{k \cdot b}{2} \cdot \sin(\theta).$$

Here, θ is the scattering angle, k is the wavenumber of the illuminating laser, and for the condition $I(\delta) = 0.5$, δ was numerically estimated to be $\delta = \pm 1.39$. The scattering angle θ is the quantity measured by the CCD camera, from which the terrace length b can be determined.

$$b = 2\frac{\delta\lambda}{\pi} \cdot \frac{1}{\sin\theta} \qquad \text{with } \frac{1}{\sin\theta} \approx \frac{l}{19\ \mu\text{m} \cdot \text{FWHM}}. \tag{1}$$

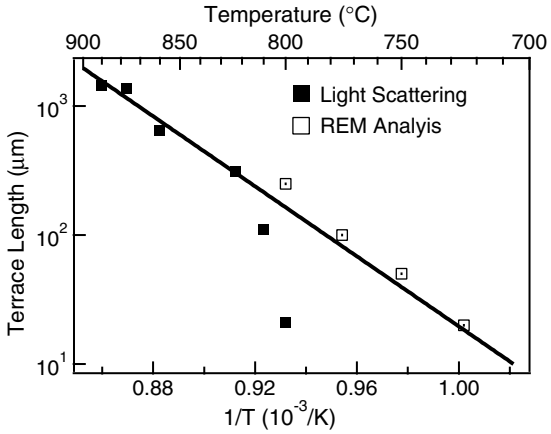

Figure 12. Arrhenius plot of the terrace length as a function of the temperature. The datapoints follow a general activated behaviour with an activation energy of $E_A = 2.8$ eV. The two light-scattering datapoints at $T \approx 800\,^{\circ}$C were not included in the fit. REM data taken from [21].

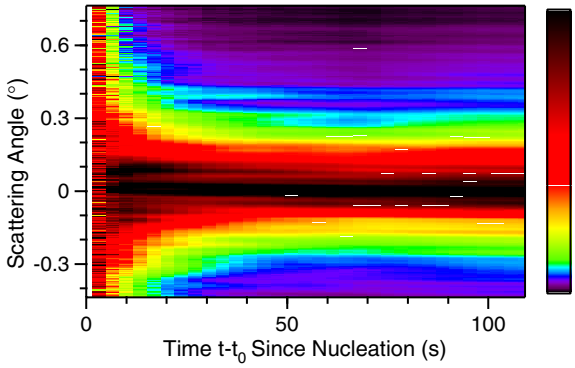

Figure 13. Averaged light scattering profiles plotted in a colour coded representation as function of the time during faceting at $T = 825\,^{\circ}$C. After initial terrace formation at t_0 the pattern gets narrower, as an indication of growing terraces.

The distance between the sample surface and the CCD camera is $l = 95$ cm, and FWHM is the full width at half maximum of the fitted Lorentz curve in pixels of the CCD camera (that needs to be multiplied with the CCD pixel size of 19 μm to obtain the correct value for θ).

While this single-slit model is obviously a tremendous simplification of the underlying physics, the speculative assumption of more complicated distribution functions for the terraces, like the geometric distribution that is popular for analysis of electron diffraction data [17], or a double-slit model that incorporates coherent nearest neighbour interaction, results in similar equations for the halfwidth, with small correction factors [21].

The simple model will now be applied to estimate the average terrace length from the CCD images. The length of terraces at different temperatures is plotted in an Arrhenius plot in figure 12. The filled squares are from the light diffraction experiment, the open squares are from a reflection electron microscopy (REM) study [20, 21]. The two light scattering datapoints below $T = 810\,^{\circ}$C that represent terraces with a length below 100 μm do not follow the general

trend. Since these terraces are already fairly small, it is questionable whether the simple data analysis still holds. Also, the halfwidth of the diffraction pattern has become so large that it is difficult to reliably determine a terrace length from the data. These two datapoints were thus excluded from the following analysis.

In the Arrhenius representation of figure 12 the remaining data points follow a straight line. A best fit with a general activated behaviour

$$b = b_0 \cdot \exp\left(-\frac{E_\mathrm{A}}{k_b \cdot T}\right)$$

gives an activation energy of $E_\mathrm{A} = 2.8$ eV for the faceting process. The good agreement with the REM datapoints gives a late justification for the simple data analysis.

If the light diffraction experiment is indeed sensitive to the average length of the terraces on the sample, it should also be possible to detect the fast expansion of the terraces along the steps of the substrate during the initial stages of the faceting. Since the integral intensity of the pattern changes significantly during the faceting (see figure 9), the averaged profiles were normalized before plotting them over time in a colour-coded representation in figure 13. The figure shows an experiment at $T = 825\,^\circ$C. At $t = 0$ s, the first (short) terraces are formed on the sample and the diffraction pattern is wider than the CCD camera. Within a few seconds the pattern becomes much narrower and pronounced maxima become apparent that are caused by the fine structure of the diffraction grating. After about 50 s the pattern does not change any more and the terraces have reached their maximum length. Some seconds later the pattern gains width again. From LEEM images at the end of the faceting, figure 2(c), and *ex situ* AFM investigations [14] it is known that during the later stages of the faceting superkinks are formed that compensate a slight azimuthal miscut of the sample. These kinks introduce a new short length scale and are believed to effectively increase the width of the diffraction pattern towards the end of the faceting.

Assuming that the terraces grow with a constant speed v at the beginning of the faceting, the terrace length b changes as $b = v \cdot (t - t_0)$, where t_0 is the moment of terrace formation. Accordingly, the FWHM can be expressed from equation (1) as

$$\mathrm{FWHM} = 2\frac{\delta\lambda}{\pi} \cdot \frac{l}{v \cdot (t - t_0)} \cdot \frac{1}{19\ \mu\mathrm{m}}. \tag{2}$$

Figure 14 shows the experimentally determined halfwidth from Figure 13 over time in a double-logarithmic plot after offset subtraction. The right axis shows the terrace length as calculated from equation (1). During the first 50 s after the terrace formation, the datapoints follow a straight line in figure 14, indicative of a terrace expansion with constant velocity. After about 50 s, the behaviour changes as the terraces start to hinder each other's expansion and kinks are formed. A fit to determine v in equation (2) during the first 50 s gives $v \approx 30\ \mu\mathrm{m\ s}^{-1}$. This value is in excellent agreement with LEEM measurements, where the initial speed of isolated terraces was determined to vary between $v_1 = 2.5\ \mu\mathrm{m\ s}^{-1}$ and $v_2 = 90\ \mu\mathrm{m\ s}^{-1}$ [18].

6. Discussion and conclusions

The simple adsorption of a submonolayer of Au on a vicinal Si(001) surface triggers the rearrangement of the surface and leads to a mesoscopic pattern. If the kinetics of the faceting are considered, it becomes clear that the two-stage faceting process must lead to long range order. The formation of (001) terraces is driven by the energy gained by formation of the (5×3.2) reconstruction on the (001) terraces. These terraces, however, can only form when the local Au coverage exceeds a critical coverage of one-third of a monolayer. Once a terrace is formed, all Au that is deposited inside a capture zone around the terrace diffuses to the

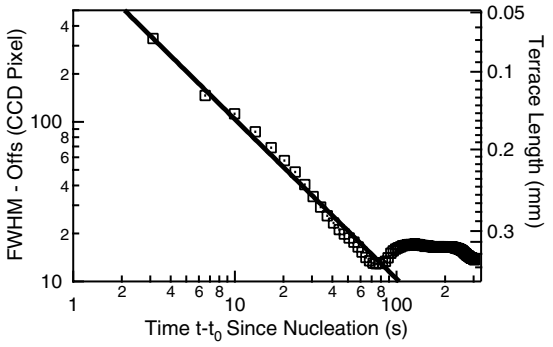

Figure 14. Time development of the terrace length over time from the data in figure 13.

terrace and is immediately incorporated. This effectively prevents formation of a new terrace in the close vicinity of the first terrace, since the local coverage in the surroundings of the terrace is below the critical coverage for terrace formation. This creates long-range order on the surface that scales with the diffusion length. Au is an excellent candidate for this, because the desorption temperature for Au on Si is fairly high and deposition can take place at high temperatures to achieve large diffusion lengths. If Ag is used for the faceting instead of Au, similar arguments may count, but faceting must take place at much lower temperature because of the lower desorption temperature of Ag. Accordingly, the largest reported periodicity of the created surface undulation is $\approx$100 nm for Ag deposition at $T = 770\,^{\circ}\mathrm{C}$ [27].

The second step of the faceting is the transformation of irregular step-bunches into facets. Since for energetic reasons the terraces cannot accumulate more Au from the surroundings, Au adsorbs on the step-band and rearranges it into a better ordered and reconstructed entity. While the (001) terraces slightly shrink during this re-ordering, the periodicity of the grating on the surface is not changed during this step.

As the dimensions of self-organized structures reach mesoscopic scales, the search for new techniques that quickly characterize the resulting surfaces becomes a pressing issue. Atomic force microscopy (AFM), and for smaller structures STM, have established themselves as excellent tools to observe the final results of self-assembly at surfaces. Both techniques, however, are rather cumbersome when it comes to *in situ* imaging of the self-ordering inside UHV during deposition. Diffraction experiments are much easier to handle in that respect, although the results are sometimes more difficult to interpret. Ultimately, a combination of various techniques is certainly favourable.

For a diffraction experiment, the wavelength of the illumination source has to be matched to the structure size on the sample. For the ordered blaze grating formed during Au induced faceting, visible light appears to be a good choice. Already a simple HeNe Laser provides the possibility to record diffraction patterns *in situ* and during deposition. The exact interpretation of the diffraction pattern requires assumptions to be made about the exact terrace distribution on the surface, and the detailed understanding of the interaction of light with rough surfaces is a research area by itself [28]. If the pattern is averaged and one does not attempt to predict the whole pattern in detail, however, a very simple slit-model can already give useful numbers for the terrace length. The results presented here fit into the general picture of the faceting and are in good agreement with results from other techniques. In that respect, light diffraction is a useful technique to monitor the development of long-range order in self-organized materials systems.

Acknowledgments

It is my pleasure to acknowledge many fruitful discussions with Michael Horn-von Hoegen and Peter Kury. I also acknowledge helpful assistance from H Minoda, Thomas Schmidt, Stefan Heun, Rüdiger Hild, Percy Zahl, Barbara Ressel and Ernst Bauer. This investigation has been supported by the Deutsche Forschungsgemeinschaft under project No H016/11-4.2 and by the European Union, proposal No 98-014.

References

[1] Suliga E and Henzler M 1983 *J. Vac. Sci. Technol.* A **1** 1507
[2] Aoki K, Suzuki T, Minoda H, Tanishiro Y and Yagi K 1998 *Surf. Sci.* **408** 101
[3] Latyshev A, Litvin L and Aseev A 1998 *Appl. Surf. Sci.* **130–132** 139
[4] Homma Y and Aizawa N 2000 *Phys. Rev.* B **62** 8323
[5] Herring C 1982 *Phys. Rev.* **82** 87
[6] Webb M 1994 *Surf. Sci.* **299/300** 454
[7] Chadi D 1987 *Phys. Rev. Lett.* **59** 1691
[8] Pehlke E and Tersoff J 1991 *Phys. Rev. Lett.* **67** 465
[9] Horn-von Hoegen M and Golla A 1996 *Phys. Rev. Lett.* **76** 2953
[10] Fölsch S, Winau D, Meyer G, Rieder K H, Horn-von Hoegen M, Schmidt T and Henzler M 1995 *Appl. Phys. Lett.* **67** 2185
[11] Meier A, Zahl P, Vockenroth R and Horn-von Hoegen M 1998 *Appl. Surf. Sci.* **123/124** 694
[12] Hild R, Seifert C, Kammler M, Meyer zu Heringdorf F-J, Horn-von Hoegen M, Zachuk R and Olshanetsky B 2002 *Surf. Sci.* **512** 117
[13] Minoda H, Shimakura T, Yagi K, Meyer zu Heringdorf F-J and Horn-von Hoegen M 1999 *Surf. Sci.* **432** 69
[14] Horn-von Hoegen M, Meyer zu Heringdorf F-J, Kähler D, Schmidt T and Bauer E 1998 *Thin Solid Films* **336** 16
[15] Scheithauer U, Meyer G and Henzler M 1986 *Surf. Sci.* **178** 441
[16] Schmidt T, Heun S, Slezak J, Diaz J and Prince K 1998 *Surf. Rev. Lett.* **5** 1287
[17] Horn-von Hoegen M 1999 *Z. Kristallogr.* **214** 591
[18] Meyer zu Heringdorf F-J, Kähler D, Horn-von Hoegen M, Schmidt T, Bauer E, Copel M and Minoda H 1998 *Surf. Rev. Lett.* **5** 1167
[19] Hild R, Meyer zu Heringdorf F-J, Zahl P and Horn-von Hoegen M 2000 *Surf. Sci.* **454–456** 851
[20] Minoda H, Yagi K, Meyer zu Heringdorf F-J, Meier A, Kähler D and Horn-von Hoegen M 1999 *Phys. Rev.* B **59** 2363
[21] Meyer zu Heringdorf F-J 1999 *PhD Thesis* University of Hannover, Germany, published online at http://www.tib.uni-hannover.de
[22] Lifshits V, Saranin A A and Katayama M 2003 *Surface Phases on Silicon* (New York: Wiley)
[23] Meyer zu Heringdorf F-J, Schmidt T, Heun S, Hild R, Zahl P, Ressel B, Bauer E and Horn-von Hoegen M 2001 *Phys. Rev. Lett.* **86** 5088
[24] Meyer zu Heringdorf F-J and Horn-von Hoegen M 2005 *Rev. Sci. Instrum.* **76** 085102
[25] Minoda H, Shimakura T, Yagi K, Meyer zu Heringdorf F-J and Horn-von Hoegen M 2000 *Phys. Rev.* B **61** 5672
[26] Hecht E 2001 *Optik* 3rd edn (Munich: Oldenbourg)
[27] Meier A, Zahl P, Vockenroth R and Horn-von Hoegen M 1997 *Appl. Surf. Sci.* **123/124** 694
[28] Ruiz-Cortès V and Dainty J 2002 *J. Opt. Soc. Am.* A **19** 2043